Computing-heightened low-cost high-dimensional controlled-SUM gates

Zhi-Guo Fan[1], Zhuo-Ya Bai[2],* Qiu-Lin Tan[1], and Fang-Fang Du[1†]
[1] *Key Laboratory of Micro/nano Devices and Systems, Ministry of Education, North University of China, Tai Yuan 030051, China and*
[2] *Beijing National Research Center for Information Science and Technology, Department of Electronic Engineering, Tsinghua University, Beijing 100084, China*
(Dated: April 25, 2025)

Qudit-based quantum gates offer several advantages over qubit-based counterparts, such as higher information density, the ability to address more complex problems, and richer quantum operations. In this paper, we present three realistic protocols for implementing a 4×4-dimensional (16D) two-qudit controlled-SUM (CSUM) gate, where the 4D control qudit and 4D target qudit are encoded in the polarization degree of freedom (DoF) and spatial DoF of two photons, respectively. The first protocol is implemented exclusively using linear optical elements without auxiliary resources, making it feasible with current optical technologies and achieving an efficiency of 1/9. The second protocol utilizes photon scattering by a microcavity-quantum-dot system, enabling the 16D CSUM gate to operate deterministically without postselection. The third protocol introduces an error-heralded mechanism based on the second protocol, theoretically achieving unity fidelity. Moreover, all protocols operate without ancillary photons, offering the advantages of compact circuits and low cost while further promoting the development of high-dimensional quantum computation.

I. INTRODUCTION

Quantum computing is increasingly recognized for its potential advantages over classical computing [1–5]. Quantum logic gates are fundamental units to quantum computing processes [6–15]. High-dimensional (HD) qudits, which extend two-dimensional qubits [16–21], significantly enhance the channel capacity of quantum resources [22, 23], enabling HD quantum information transmission [24–30] and potentially facilitating fault-tolerant quantum computing [31] and distributed quantum networks [32–35]. In HD space, qudit systems offer great flexibility for information storage and processing, including simplified quantum gates [36], improved information security [37–43], and the exploration of unique quantum properties [44, 45]. Beyond quantum computing, qudits offer benefits in quantum communication due to their superior noise resilience [46–51] and their ability to support higher key rates [52–56].

Reliable quantum computing necessitates high-fidelity quantum logic gates. The controlled-NOT (CNOT) gate, in particular, is extensively utilized in quantum computing for applications, such as quantum algorithms [57–59], error correction [31], arithmetic operations [60, 61], and fault-tolerant computing [62–64]. As circuit complexity grows, the limitations of traditional low-dimensional CNOT gates become more pronounced, increasing the demand for design of HD counterpart gates, i,e., controlled-SUM (CSUM) gates. In the $d \times d$-D ($d > 2$) Hilbert space, the $d \times d$-D CSUM gate can be expressed as $U^d_{\rm CSUM}|c,t\rangle = |c,(c+t)\%d\rangle$, where $c,t \in \{0,1,...,d-1\}$. It is evident that the CNOT gate is a special case of the CSUM gate when $d = 2$. Especially, the 4×4-D (16D) CSUM gate ($d = 4$) performs the following transformation:

$$
\begin{aligned}
&|0,0\rangle \to |0,0\rangle, |0,1\rangle \to |0,1\rangle, |0,2\rangle \to |0,2\rangle, |0,3\rangle \to |0,3\rangle,\\
&|1,0\rangle \to |1,1\rangle, |1,1\rangle \to |1,2\rangle, |1,2\rangle \to |1,3\rangle, |1,3\rangle \to |1,0\rangle,\\
&|2,0\rangle \to |2,2\rangle, |2,1\rangle \to |2,3\rangle, |2,2\rangle \to |2,0\rangle, |2,3\rangle \to |2,1\rangle,\\
&|3,0\rangle \to |3,3\rangle, |3,1\rangle \to |3,0\rangle, |3,2\rangle \to |3,1\rangle, |3,3\rangle \to |3,2\rangle.
\end{aligned}
$$

Photon systems possess inherent immunity to decoherence and offer multiple accessible degrees of freedom (DoF), making them well-suited for encoding qudit information [65–70]. These advantages make the HD CSUM gate implemented exclusively by linear optical elements easier to realize. Recently, many CSUM gates have been proposed in quantum information processing (QIP). In 2019, Imany *et al.* proposed a 3×3-D CSUM gate with a fidelity exceeding 0.90, utilizing time and frequency DoF for encoding [71]. In 2020, Gao *et al.* implemented a 3×3-D CSUM gate with the assistance of a three-photon entangled state, achieving an efficiency of 1/152 [72]. In 2022, Su *et al.* reported a 3×3-D hybrid CSUM gate with one superconducting qutrit and a cat-state qutrit [73]. In 2024, a 2×4-D polarization-spatial CSUM gate, with an average fidelity and efficiency exceeding 0.99, was realized by Meng *et al.*[74]. Most qudit-based gates offer several advantages over qubit-based counterparts, such as shorter computation times, reduced resource requirements, greater availability, and the capacity to address more complex problems. Overall, research on HD quantum gates broadens the current quantum computing framework [75].

In this paper, we present three useful protocols to set up the 16D two-qudit CSUM gate, where the 4D control qudit and 4D target qudit of the CSUM gate are encoded in the polarization DoF and spatial DoF of two photons, respectively. The first protocol employs linear optical elements achieving an efficiency of 1/9, which beats

* zybai@mail.tsinghua.edu.cn
† Duff@nuc.edu.cn

the 3×3-D CSUM gate with the efficiency of 1/152 assisted by the three-photon entangled state [72]. The second protocol is implemented through photon scattering off a microcavity-quantum-dot (microcavity-QD) system, where it operates deterministically. The third protocol introduces an error-heralded framework on the foundation of the second protocol, elevating the fidelity of the 16D CSUM gate near unity, in principle. Moreover, each protocol can requires no ancillary photons, offering the advantages of compact circuits and low cost.

The paper is organized as follows. In Sec. II, the first 16D CSUM gate protocol with linear optical elements is presented. In Sec. III, the second protocol implemented by the photon scattering property off microcavity-QD system is implemented. The third protocol that introduces an error-heralded mechanism based on the second protocol is showed in Sec. IV. We provide a detailed discussion on the fidelity and efficiency of each protocol in Sec. V and a summary in Sec. VI.

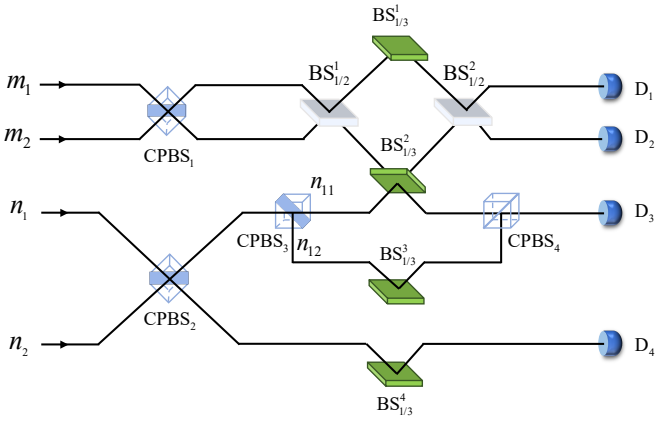

FIG. 1. Schematic diagram of 16D CSUM gate implemented with linear optics. CPBS denotes a circular polarization beam splitter, which transmit (reflect) the $|R\rangle-$ ($|L\rangle$-) polarization state of the photon. $BS_{1/2}$ is a 1/2-reflectivity beam splitter. $BS_{1/3}$ is a 1/3-reflectivity beam splitter. D is a single-photon detector.

II. THE 16D CSUM GATE IMPLEMENTED WITH LINEAR OPTICS

The schematic diagram of the first protocol for the 16D CSUM gate implemented with linear optics is illustrated in Fig. 1. The initial states of the two photons, labeled M and N, in both polarization and spatial DoFs, are

$$\begin{aligned} |\varphi\rangle^P_{MN} &= (\alpha_1|LL\rangle + \beta_1|LR\rangle + \gamma_1|RL\rangle + \delta_1|RR\rangle)_{MN}, \\ |\varphi\rangle^S_{MN} &= (\alpha_2|m_1n_1\rangle + \beta_2|m_1n_2\rangle + \gamma_2|m_2n_1\rangle \\ &\quad +\delta_2|m_2n_2\rangle)_{MN}, \end{aligned} \tag{1}$$

where the coefficients adhere the normalization condition $|\alpha_i|^2 + |\beta_i|^2 + |\gamma_i|^2 + |\delta_i|^2 = 1$ for $i = 1, 2$. Thus, the initial states of the entire system can be expressed as $|\Psi_0\rangle = |\varphi\rangle^P_{MN} \otimes |\varphi\rangle^S_{MN}$.

Firstly, two photons M and N in spatial modes m_1, m_2, n_1, and n_2 pass through respective circular polarized beam splitters ($CPBS_1$ and $CPBS_2$), which transmit (reflect) the $|R\rangle$ ($|L\rangle$) polarization state of the photon. Owing to the property of the CPBS, only the spatial modes entangled with $|R\rangle$-polarized photons are exchanged, resulting in

$$\begin{aligned} |\Psi_1\rangle &= \alpha_1|LL\rangle_{MN} \otimes (\alpha_2|m_1n_1\rangle + \beta_2|m_1n_2\rangle + \gamma_2|m_2n_1\rangle \\ &\quad +\delta_2|m_2n_2\rangle) + \beta_1|LR\rangle_{MN} \otimes (\alpha_2|m_1n_2\rangle \\ &\quad +\beta_2|m_1n_1\rangle + \gamma_2|m_2n_2\rangle + \delta_2|m_2n_1\rangle) + \gamma_1|RL\rangle_{MN} \\ &\quad \otimes(\alpha_2|m_2n_1\rangle + \beta_2|m_2n_2\rangle + \gamma_2|m_1n_1\rangle + \delta_2|m_1n_2\rangle) \\ &\quad +\delta_1|RR\rangle_{MN} \otimes (\alpha_2|m_2n_2\rangle + \beta_2|m_2n_1\rangle \\ &\quad +\gamma_2|m_1n_2\rangle + \delta_2|m_1n_1\rangle). \end{aligned} \tag{2}$$

Secondly, for the spatial mode of photon M, an interferometric network is constructed using two 1/2-reflectivity beam splitters ($BS^1_{1/2}$ and $BS^2_{1/2}$), while two 1/3-reflectivity beam splitters ($BS^1_{1/3}$ and $BS^2_{1/3}$) are positioned on the two arms of the interferometer, respectively. The $BS_{1/2}$ applies the operation to two spatial modes of the photon M, i.e., $|m_1\rangle = (|m_1\rangle + |m_2\rangle)/\sqrt{2}$ and $|m_2\rangle = (|m_1\rangle - |m_2\rangle)/\sqrt{2}$. For photon N, after passing through the $CPBS_3$, its spatial mode n_1 is split into the spatial modes n_{11} and n_{12}. These modes are subsequently recombined into the spatial mode n_1 by $CPBS_4$. The photon M in the spatial mode m_2 and the photon N in the spatial mode n_{11} simultaneously pass through the $BS^2_{1/3}$. This induces interference between the two photons, resulting in a π-phase shift in the interferometric arms [76]. It is noteworthy that the $BS^1_{1/3}$, $BS^3_{1/3}$, and $BS^4_{1/3}$ in proper order the m_1, n_{12}, and n_2 spatial modes do not participate in the interference between two photons but serves to average the photon loss. After these operation, the state of the entire system is evolved to

$$\begin{aligned} |\Psi_2\rangle &= \frac{1}{3}\{\alpha_1|LL\rangle_{MN} \otimes (\alpha_2|m_1n_1\rangle + \beta_2|m_1n_2\rangle \\ &\quad +\gamma_2|m_2n_1\rangle + \delta_2|m_2n_2\rangle) + \beta_1|LR\rangle_{MN} \\ &\quad \otimes(\alpha_2|m_1n_2\rangle + \beta_2|m_2n_1\rangle + \gamma_2|m_2n_2\rangle \\ &\quad +\delta_2|m_1n_1\rangle) + \gamma_1|RL\rangle_{MN} \otimes (\alpha_2|m_2n_1\rangle \\ &\quad +\beta_2|m_2n_2\rangle + \gamma_2|m_1n_1\rangle + \delta_2|m_1n_2\rangle) \\ &\quad +\delta_1|RR\rangle_{MN} \otimes (\alpha_2|m_2n_2\rangle + \beta_2||m_1n_1\rangle \\ &\quad +\gamma_2|m_1n_2\rangle + \delta_2|m_2n_1\rangle)\}. \end{aligned} \tag{3}$$

In Eq. (3), we retain only the photon-number-conserving terms detectable by photon detector D, while omitting the failure modes of the CSUM gate where the output ports of the single photon do not each contain exactly one photon. Comparing Eq. (2) with Eq. (3), it can be seen that, when photon N is in the $|Rn_1\rangle_N$ state, the $|m_1\rangle$ component of photon M is converted into $|m_2\rangle$ one and vice versa. In all other cases, the states of two photons N and M remain unchanged.

The polarization states of two photons M and N are served as the 4D control qudit, that is, $|LL\rangle \rightarrow$

$|\bar{0}\rangle_c, |LR\rangle \rightarrow |\bar{1}\rangle_c, |RL\rangle \rightarrow |\bar{2}\rangle_c$, and $|RR\rangle \rightarrow |\bar{3}\rangle_c$. Simultaneously, the spatial states of two photons M and N are worked as 4D target qudit, that is, $|m_1 n_1\rangle \rightarrow |\bar{0}\rangle_t, |m_1 n_2\rangle \rightarrow |\bar{1}\rangle_t, |m_2 n_1\rangle \rightarrow |\bar{2}\rangle_t, |m_2 n_2\rangle \rightarrow |\bar{3}\rangle_t$. Consequently, the 16D CSUM gate can be successfully implemented with linear optical elements, i.e.,

$$\begin{aligned}|\mathrm{CSUM}\rangle \;=\; & \frac{1}{3}\{\alpha_1|\bar{0}\rangle_c \otimes (\alpha_2|\bar{0}\rangle_t + \beta_2|\bar{1}\rangle_t + \gamma_2|\bar{2}\rangle_t \\ & +\delta_2|\bar{3}\rangle_t) + \beta_1|\bar{1}\rangle_c \otimes (\alpha_2|\bar{1}\rangle_t + \beta_2|\bar{2}\rangle_t \\ & +\gamma_2|\bar{3}\rangle_t + \delta_2|\bar{0}\rangle_t) + \gamma_1|\bar{2}\rangle_c \otimes (\alpha_2|\bar{2}\rangle_t \\ & +\beta_2|\bar{3}\rangle_t + \gamma_2|\bar{0}\rangle_t + \delta_2|\bar{1}\rangle_t) + \delta_1|\bar{3}\rangle_c \\ & \otimes(\alpha_2|\bar{3}\rangle_t + \beta_2|\bar{0}\rangle_t + \gamma_2|\bar{1}\rangle_t + \delta_2|\bar{2}\rangle_t)\}. \quad (4)\end{aligned}$$

It is evident that the efficiency η_1 of 16D CSUM gate with linear optics is 1/9. We have completed the first protocol by encoding information in the spatial and polarized DoFs of two flying photons, resulting in significant resource savings.

III. THE DETERMINISTIC 16D CSUM GATE ASSISTED BY TWO ONE-SIDED MICROCAVITY-QD SYSTEMS

As illustrated top left in Fig. 2, the microcavity-QD system, which consists of a singly charged In(Ga)As QD embedded within an optically resonant single-sided microcavity. The four-level emitter configuration comprises ground states $|\downarrow\rangle$ and $|\uparrow\rangle$.This configuration additionally integrates two optically excited X^- trion states, labeled as $|\uparrow\downarrow\Uparrow\rangle$ and $|\downarrow\uparrow\Downarrow\rangle$.As governed by selection rules, the QD spin states $|\downarrow\rangle$ and $|\uparrow\rangle$ couple to left- (L) and right- (R) circularly polarized photons, respectively. This coupling facilitates optical transitions to the respective trion states. A $|R\rangle$- or $|L\rangle$-polarized photon at frequency ω, which enters via the input mode $\hat{a}^\dagger_{\mathrm{in},\omega}$, interacts with the microcavity-QD system and propagates to the output mode $\hat{a}^\dagger_{\mathrm{out},\omega}$. Under adiabatic cavity-field evolution under negligible QD excitation, the quantum state-dependent reflection coefficient r_e ($e = 0, 1$) is

$$r_e(\omega) \;=\; 1 - \frac{\kappa f}{eg^2 + [-(\omega-\omega_c)i + \frac{\kappa}{2} + \frac{\kappa_s}{2}]f}, \quad (5)$$

here, $e = 1$ describes the interaction in the coupled microcavity-QD system with the polarized photon, whereas $e = 0$ corresponds to the interaction in the uncoupled microcavity configuration. The parameter g denotes the cavity-X^--trion coupling strength. The parameter κ is the directional coupling rate, governing energy transfer dynamics within the system. κ_s corresponds to the cavity-side leakage rate, and γ represents the spontaneous emission rate of the trion. The f is $\gamma/2-(\omega-\omega_{X^-})i$, in which ω_{X^-} and ω_c are the transition frequency of the QD and the cavity resonance frequency, respectively. For simplicity, we assume $\omega_{X^-} = \omega_c$ (resonant condition). Under realistic conditions, the state-selective reflection coefficient for the input photon interacting with the one-sided microcavity-QD system is expressed as

$$\begin{aligned}&|L\rangle|\uparrow\rangle \rightarrow r_1|L\rangle|\uparrow\rangle, \quad |L\rangle|\downarrow\rangle \rightarrow r_0|L\rangle|\downarrow\rangle, \\ &|R\rangle|\downarrow\rangle \rightarrow r_1|R\rangle|\downarrow\rangle, \quad |R\rangle|\uparrow\rangle \rightarrow r_0|R\rangle|\uparrow\rangle. \quad (6)\end{aligned}$$

In the condition $\kappa \gg \kappa_s$ and $g^2 \gg \kappa\gamma$, the coupling and uncoupling reflection coefficients become $r \approx 1$ and $r_0 \approx -1$, leading to the rules

$$\begin{aligned}&|L\rangle|\uparrow\rangle \rightarrow |L\rangle|\uparrow\rangle, \quad |L\rangle|\downarrow\rangle \rightarrow -|L\rangle|\downarrow\rangle, \\ &|R\rangle|\downarrow\rangle \rightarrow |R\rangle|\downarrow\rangle, \quad |R\rangle|\uparrow\rangle \rightarrow -|R\rangle|\uparrow\rangle. \quad (7)\end{aligned}$$

Now we introduce the second protocol for deterministic 16D CSUM gate, which is assisted by two one-sided microcavity-QD systems. The deterministic 16D CSUM gate is completed with two steps. The first step performs the 4D qudit-flip operation for the 4D target qudit, while the second step serves as a spatial-mode coupler, merging the previously separated four spatial modes into two. Under these two basic steps, the second protocol is readily implemented.

The quantum circuit for the first step of the deterministic 16D CSUM gate is illustrated in the left part of Fig. 2. The initial states of the two photons, labeled M and N, in both polarization and spatial DoFs, are $|\Psi_0\rangle$. The auxiliary electron spin of the QD_j-microcavity system is initialized as $|+\rangle_j = \frac{1}{\sqrt{2}}(|\uparrow\rangle + |\downarrow\rangle)_j$, where $j = 1, 2$ (i.e., QD_1 of the first step and QD_2 of the second step). Thus, the initial states of the entire system can be expressed as $|\Phi_0\rangle = |\Psi_0\rangle \otimes |+\rangle_1 \otimes |+\rangle_2$.

Foremostly, similar to the first step of the first protocol, two photons M and N in spatial modes m_1, m_2, n_1, and n_2 pass through the CPBS_1 and CPBS_2, resulting in $|\Phi_1\rangle = |\Psi_1\rangle \otimes |+\rangle_1 \otimes |+\rangle_2$, where $|\Psi_1\rangle$ in Eq. (2). After that, photon M in spatial mode m_1 or m_2 passes through $\mathrm{BS}^1_{1/2}$ or $\mathrm{BS}^2_{1/2}$, which apply the operation to two spatial modes of the photon, i.e., $|m_1\rangle = (|m_{11}\rangle + |m_{12}\rangle)/\sqrt{2}$ and $|m_2\rangle = (|m_{21}\rangle + |m_{22}\rangle)/\sqrt{2}$. Then the spatial mode of photon N (M) through CPBS_5 (CPBS_3 or CPBS_4) is split into two polarization-depended spatial modes. Subsequently, the $|L\rangle_M|L\rangle_N$ polarization states of two photons in spatial modes m^1_{11} (or m^1_{21}), and n_{11} pass directly interact with the microcavity-QD_1 system via the rules in Eq. (7), while their $|R\rangle_M|R\rangle_N$ states in spatial modes m^2_{11} (or m^2_{21}), and n_{12} pass sequentially through X_1 (or X_2), $\mathrm{X}_3 \rightarrow$ microcavity-QD_1 system$\rightarrow$ X_4 (or X_5), X_6. Here, the operator $\mathrm{X_k}$ ($k = 1, 2, ..., 6$) is a half-wave plate executing a qubit-flip function on the P photon, where $\sigma^P_x = |R\rangle_P\langle L| + |L\rangle_P\langle R|$ for $P = M, N$. Finally, CPBS_6 and CPBS_7 combine the four spatial modes of photon M separated by CPBS_3 and CPBS_4. The hybrid state of

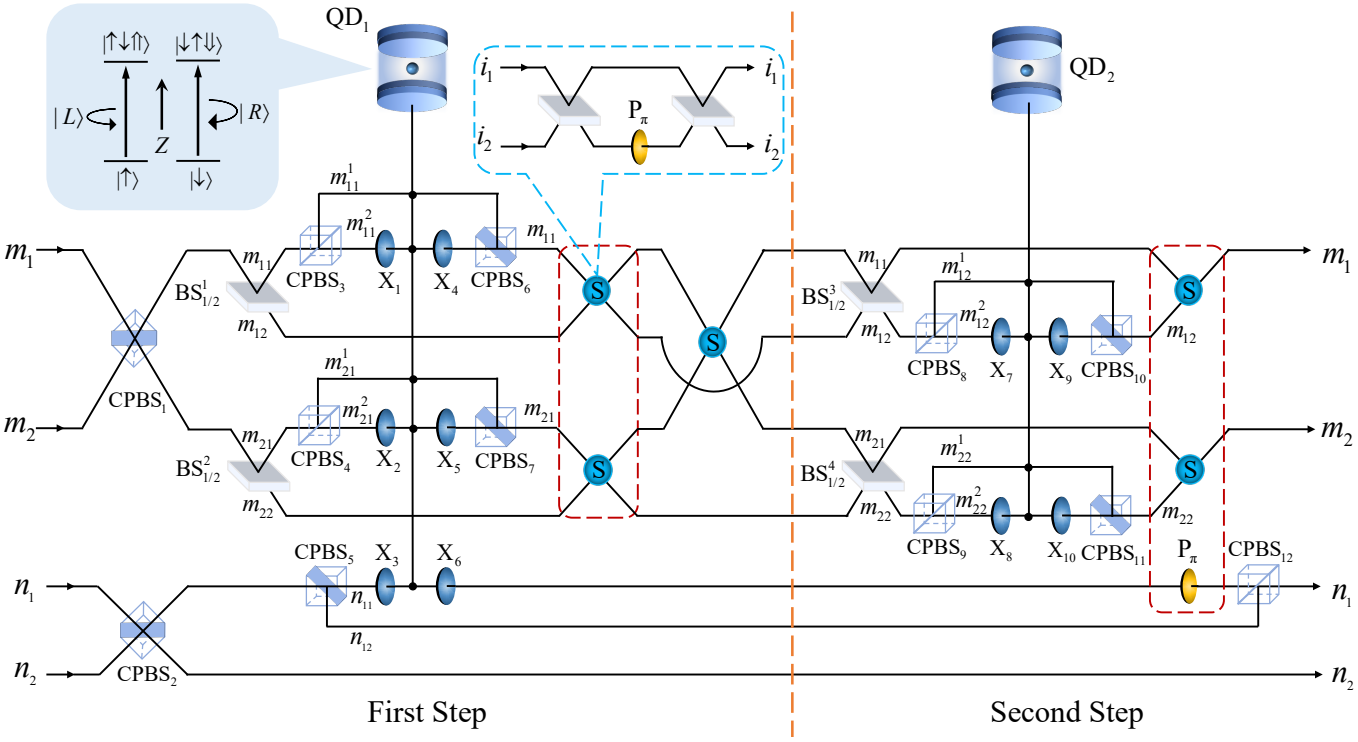

FIG. 2. Schematic diagram of the deterministic 16D CSUM gate assisted by the one-sided microcavity-QD system. $X_k (k = 1, 2, ...6)$ represents qubit-flip function on P photon, i.e., $\sigma_x^P = |R\rangle_P\langle L| + |L\rangle_P\langle R| (P = M, N)$. P_π denotes the phase shifter, performing the transformation, i.e., $|R\rangle\,(|L\rangle) \to -|R\rangle\,(-|L\rangle)$.

two photons and electron spin is represented as

$$\begin{aligned}|\Phi_2\rangle \;=\; & [\alpha_1|LL\rangle_{MN}\otimes(\alpha_2|m_{12}n_{12}\rangle+\beta_2|m_{12}n_2\rangle\\ & +\gamma_2|m_{22}n_{12}\rangle+\delta_2|m_{22}n_2\rangle)+\beta_1|LR\rangle_{MN}\\ & \otimes(\alpha_2|m_{12}n_2\rangle+\beta_2|m_{11}n_{11}\rangle+\gamma_2|m_{22}n_2\rangle\\ & +\delta_2|m_{21}n_{11}\rangle)+\gamma_1|RL\rangle_{MN}\otimes(\alpha_2|m_{22}n_{12}\rangle\\ & +\beta_2|m_{22}n_2\rangle+\gamma_2|m_{12}n_{12}\rangle+\delta_2|m_{12}n_2\rangle)\\ & +\delta_1|RR\rangle_{MN}\otimes(\alpha_2|m_{22}n_2\rangle+\beta_2|m_{21}n_{11}\rangle\\ & +\gamma_2|m_{12}n_2\rangle+\delta_2|m_{11}n_{11}\rangle)]\otimes|+\rangle_1\otimes|+\rangle_2\\ & +[\alpha_1|LL\rangle_{MN}\otimes(\alpha_2|m_{11}n_{12}\rangle+\beta_2|m_{11}n_2\rangle\\ & +\gamma_2|m_{21}n_{12}\rangle+\delta_2|m_{21}n_2\rangle)+\beta_1|LR\rangle_{MN}\\ & \otimes(\alpha_2|m_{11}n_2\rangle+\beta_2|m_{12}n_{11}\rangle+\gamma_2|m_{21}n_2\rangle\\ & +\delta_2|m_{22}n_{11}\rangle)+\gamma_1|RL\rangle_{MN}\otimes(\alpha_2|m_{21}n_{12}\rangle\\ & +\beta_2|m_{21}n_2\rangle+\gamma_2|m_{11}n_{12}\rangle+\delta_2|m_{11}n_2\rangle)\\ & +\delta_1|RR\rangle_{MN}\otimes(\alpha_2|m_{21}n_2\rangle+\beta_2|m_{22}n_{11}\rangle\\ & +\gamma_2|m_{11}n_2\rangle+\delta_2|m_{12}n_{11}\rangle)]\otimes|-\rangle_1\otimes|+\rangle_2, \quad (8)\end{aligned}$$

$|-\rangle_j = \frac{1}{\sqrt{2}}(|\uparrow\rangle - |\downarrow\rangle)_j (j = 1)$. Then the spin state of the microcavity-QD_1 system is measured with the basis $\{|+\rangle_1, |-\rangle_1\}$. If the spin is found in state $|+\rangle_1$, the state

$$\begin{aligned}|\Phi_3\rangle \;=\; & [\alpha_1|LL\rangle_{MN}\otimes(\alpha_2|m_{12}n_{12}\rangle+\beta_2|m_{12}n_2\rangle\\ & +\gamma_2|m_{22}n_{12}+\delta_2|m_{22}n_2\rangle))+\beta_1|LR\rangle_{MN}\\ & \otimes(\alpha_2|m_{12}n_2\rangle+\beta_2|m_{11}n_{11}\rangle+\gamma_2|m_{22}n_2\rangle\\ & +\delta_2|m_{21}n_{11}\rangle)+\gamma_1|RL\rangle_{MN}\otimes(\alpha_2|m_{22}n_{12}\rangle\\ & +\beta_2|m_{22}n_2\rangle+\gamma_2|m_{12}n_{12}\rangle+\delta_2|m_{12}n_2\rangle)\\ & +\delta_1|RR\rangle_{MN}\otimes(\alpha_2|m_{22}n_2\rangle+\beta_2|m_{21}n_{11}\rangle\\ & +\gamma_2|m_{12}n_2\rangle+\delta_2|m_{11}n_{11}\rangle)]\otimes|+\rangle_2 \quad (9)\end{aligned}$$

is obtained. Otherwise, if the spin is in state $|-\rangle_1$, the related feed-forward operation with two swap (S) gates fulfilling by two $BSs_{1/2}$ and a phase shifter σ_z, executing the unitary operator $\sigma^S = |m_{q1}\rangle\langle m_{q2}| + |m_{q2}\rangle\langle m_{q1}|, (q = 1, 2)$ on two spatial modes, is applied to photon M to get the desired state $|\Phi_3\rangle$ in Eq. (9). Finally, photon M in spatial modes m_{11} and m_{21} undergoes another S to exchange two spatial modes, leading to

$$\begin{aligned}|\Phi_4\rangle \;=\; & [\alpha_1|LL\rangle_{MN}\otimes(\alpha_2|m_{12}n_{12}\rangle+\beta_2|m_{12}n_2\rangle\\ & +\gamma_2|m_{22}n_{12}\rangle+\delta_2|m_{22}n_2\rangle)+\beta_1|LR\rangle_{MN}\\ & \otimes(\alpha_2|m_{12}n_2\rangle+\beta_2|m_{11}n_{11}\rangle+\gamma_2|m_{22}n_2\rangle\\ & +\delta_2|m_{21}n_{11}\rangle)+\gamma_1|RL\rangle_{MN}\otimes(\alpha_2|m_{22}n_{12}\rangle\\ & +\beta_2|m_{22}n_2\rangle+\gamma_2|m_{12}n_{12}\rangle+\delta_2|m_{12}n_2\rangle)\\ & +\delta_1|RR\rangle_{MN}\otimes(\alpha_2|m_{22}n_2\rangle+\beta_2|m_{21}n_{11}\rangle\\ & +\gamma_2|m_{12}n_2\rangle+\delta_2|m_{11}n_{11}\rangle)]\otimes|+\rangle_2. \quad (10)\end{aligned}$$

Upon completing first step, the target qudit reaches the desired state.

The quantum circuit for the second step of the deterministic 16D CSUM gate is illustrated in the right part of Fig. 2. Firstly, photon M passes through $\mathrm{BS}^3_{1/2}$ or $\mathrm{BS}^4_{1/2}$, namely, $|m_{q1}\rangle = (|m_{q1}\rangle + |m_{q2}\rangle)/\sqrt{2}$ and $|m_{q2}\rangle = (|m_{q1}\rangle - |m_{q2}\rangle)/\sqrt{2}, (q = 1, 2)$. Subsequently, photon M in spatial modes m_{12} and m_{22} undergoes the processes, that is, passing through CPBS_8 (CPBS_9), interacting with the microcavity-QD_2 system, and converging at CPBS_{10} (CPBS_{11}), the same as the former microcavity-QD_1 system, thereby resulting in the state $|\Phi_4\rangle$ transformed into

$$\begin{aligned}|\Phi_5\rangle &= [\alpha_1|LL\rangle_{MN}\otimes(\alpha_2|m_{11}n_{12}\rangle+\beta_2|m_{11}n_2\rangle\\ &+\gamma_2|m_{21}n_{12}\rangle+\delta_2|m_{21}n_2\rangle)+\beta_1|LR\rangle_{MN}\\ &\otimes(\alpha_2|m_{11}n_2\rangle+\beta_2|m_{21}n_{11}\rangle+\gamma_2|m_{21}n_2\rangle\\ &+\delta_2|m_{11}n_{11}\rangle)+\gamma_1|RL\rangle_{MN}\otimes(\alpha_2|m_{21}n_{12}\rangle\\ &+\beta_2|m_{21}n_2\rangle+\gamma_2|m_{11}n_{12}\rangle+\delta_2|m_{11}n_2\rangle)\\ &+\delta_1|RR\rangle_{MN}\otimes(\alpha_2|m_{21}n_2\rangle+\beta_2||m_{11}n_{11}\rangle\\ &+\gamma_2|m_{11}n_2\rangle+\delta_2|m_{21}n_{11}\rangle)]\otimes|+\rangle_2\\ &-[\alpha_1|LL\rangle_{MN}\otimes(\alpha_2|m_{12}n_{12}\rangle+\beta_2|m_{12}n_2\rangle\\ &+\gamma_2|m_{22}n_{12}\rangle+\delta_2|m_{22}n_2\rangle)+\beta_1|LR\rangle_{MN}\\ &\otimes(\alpha_2|m_{12}n_2\rangle-\beta_2|m_{22}n_1\rangle+\gamma_2|m_{22}n_2\rangle\\ &-\delta_2|m_{12}n_{11}\rangle)+\gamma_1|RL\rangle_{MN}\otimes(\alpha_2|m_{22}n_1\rangle\\ &+\beta_2|m_{22}n_2\rangle+\gamma_2|m_{12}n_{11}\rangle+\delta_2|m_{12}n_2\rangle)\\ &+\delta_1|RR\rangle_{MN}\otimes(\alpha_2|m_{22}n_2\rangle-\beta_2|m_{12}n_{12}\rangle\\ &+\gamma_2|m_{12}n_2\rangle-\delta_2|m_{22}n_{12}\rangle)]\otimes|-\rangle_2. \qquad (11)\end{aligned}$$

Then the spin state of the microcavity-QD_2 system is measured with the basis $\{|+\rangle_2, |-\rangle_2\}$. If the spin is found in state $|+\rangle_2$, the state

$$\begin{aligned}|\Phi_6\rangle &= \alpha_1|LL\rangle_{MN}\otimes(\alpha_2|m_{11}n_{12}\rangle+\beta_2|m_{11}n_2\rangle\\ &+\gamma_2|m_{21}n_{12}\rangle+\delta_2|m_{21}n_2\rangle)+\beta_1|LR\rangle_{MN}\\ &\otimes(\alpha_2|m_{11}n_2\rangle+\beta_2|m_{21}n_{11}\rangle+\gamma_2|m_{21}n_2\rangle\\ &+\delta_2|m_{11}n_{11}\rangle)+\gamma_1|RL\rangle_{MN}\otimes(\alpha_2|m_{21}n_{12}\rangle\\ &+\beta_2|m_{21}n_2\rangle+\gamma_2|m_{11}n_{12}\rangle+\delta_2|m_{11}n_2\rangle)\\ &+\delta_1|RR\rangle_{MN}\otimes(\alpha_2|m_{21}n_2\rangle+\beta_2||m_{11}n_{11}\rangle\\ &+\gamma_2|m_{11}n_2\rangle+\delta_2|m_{21}n_{11}\rangle). \qquad (12)\end{aligned}$$

is obtained. Apparently, the deterministic 16D CSUM gate is successfully constructed. On the contrary, if the spin is in state $|-\rangle_2$, the related feed-forward operation assisted by two S gates on two pairs of spatial modes of photon M, m_{12} and m_{11}, m_{22} and m_{21}, is applied to photon M to get the desired state $|\Psi_6\rangle$ in Eq. (12). Thus, two spatial modes m_{11} and m_{12} (m_{21} and m_{22}) are coupled to one spatial mode m_1 (m_2). Additionally, photon N in spatial mode n_{11} should pass through a P_π operation. Finally, two spatial modes n_{11} and n_{12} of photon N converge into spatial modes n_1 through CPBS_{12}. The entire system state is transformed into

$$\begin{aligned}|\Phi_7\rangle &= \alpha_1|LL\rangle_{MN}\otimes(\alpha_2|m_1n_1\rangle+\beta_2|m_1n_2\rangle\\ &+\gamma_2|m_2n_1\rangle+\delta_2|m_2n_2\rangle)+\beta_1|LR\rangle_{MN}\\ &\otimes(\alpha_2|m_1n_2\rangle+\beta_2|m_2n_1\rangle+\gamma_2|m_2n_2\rangle\\ &+\delta_2|m_1n_1\rangle)+\gamma_1|RL\rangle_{MN}\otimes(\alpha_2|m_2n_1\rangle\\ &+\beta_2|m_2n_2\rangle+\gamma_2|m_1n_1\rangle+\delta_2|m_1n_2\rangle)\\ &+\delta_1|RR\rangle_{MN}\otimes(\alpha_2|m_2n_2\rangle+\beta_2||m_1n_1\rangle\\ &+\gamma_2|m_1n_2\rangle+\delta_2|m_2n_1\rangle)\\ &= \alpha_1|\bar{0}\rangle_c\otimes(\alpha_2|\bar{0}\rangle_t+\beta_2|\bar{1}\rangle_t+\gamma_2|\bar{2}\rangle_t\\ &+\delta_2|\bar{3}\rangle_t)+\beta_1|\bar{1}\rangle_c\otimes(\alpha_2|\bar{1}\rangle_t+\beta_2|\bar{2}\rangle_t\\ &+\gamma_2|\bar{3}\rangle_t+\delta_2|\bar{0}\rangle_t)+\gamma_1|\bar{2}\rangle_c\otimes(\alpha_2|\bar{2}\rangle_t\\ &+\beta_2|\bar{3}\rangle_t+\gamma_2|\bar{0}\rangle_t+\delta_2|\bar{1}\rangle_t)+\delta_1|\bar{3}\rangle_c\\ &\otimes(\alpha_2|\bar{3}\rangle_t+\beta_2|\bar{0}\rangle_t+\gamma_2|\bar{1}\rangle_t+\delta_2|\bar{2}\rangle_t). \qquad (13)\end{aligned}$$

We have proposed the second protocol to implement the deterministic 16D CSUM gate assisted by the photon scattering property in the two QD-microcavity systems.

IV. THE ERROR-HERALDED DETERMINISTIC 16D CSUM GATE

The fidelity of deterministic 16D CSUM gate assisted by the one-sided microcavity-QD system is affected by non-ideal scattering, including defective coupling between the cavity mode and the QD and minor side-cavity leakage, leading to a fidelity less than unity. To address this, we propose the third protocol, i.e., an error-heralded deterministic 16D CSUM gate shown in Fig. 3, where erroneous components are passively filtered by the CPBS, and error prediction is achieved using a single-photon detector (D), resulting in unity fidelity with ignoring photon loss. Compared with the above CSUM gate in Eq. (13) formed in Fig. 2, the quantum circuit of the error-heralded deterministic 16D CSUM gate shown in Fig. 3, replaces the QD_j-microcavity system with the error-heralded QD_j unit and adds some wave-front correctors (WFCs) to designated spatial modes, where the photon does not interact with the error-heralded QD_j unit during each interaction. WFC executes the coefficient variation $|R\rangle$ ($|L\rangle$) $\rightarrow A|R\rangle(|L\rangle)$. As the $|L\rangle$-polarized photon traverses error-heralded QD_j unit, it encounters various optical elements, that is, H_1 (H_3) $\rightarrow$ microcavity-QD_j system via the rules in Eq. (6)$\rightarrow$ H_2 (H_4). Here, the operator H_i (for $i = 1, 2, 3, 4$) denotes a half-wave plate that implements the Hadamard transformation on the photon's polarization DoF, such that $|L\rangle \rightarrow (|R\rangle - |L\rangle)/\sqrt{2}$ and $|R\rangle \rightarrow (|R\rangle + |L\rangle)/\sqrt{2}$. As a result of these operations, the system evolves into

$$|L\rangle|+\rangle \rightarrow A|R\rangle|-\rangle + B|L\rangle|+\rangle, \qquad (14)$$

where A and B are expressed as $(r_1 - r_0)/2$ and $(r_1 + r_0)/2$, respectively. As governed by Eq. (14), an input $|L\rangle$-polarized photon generates two distinct output

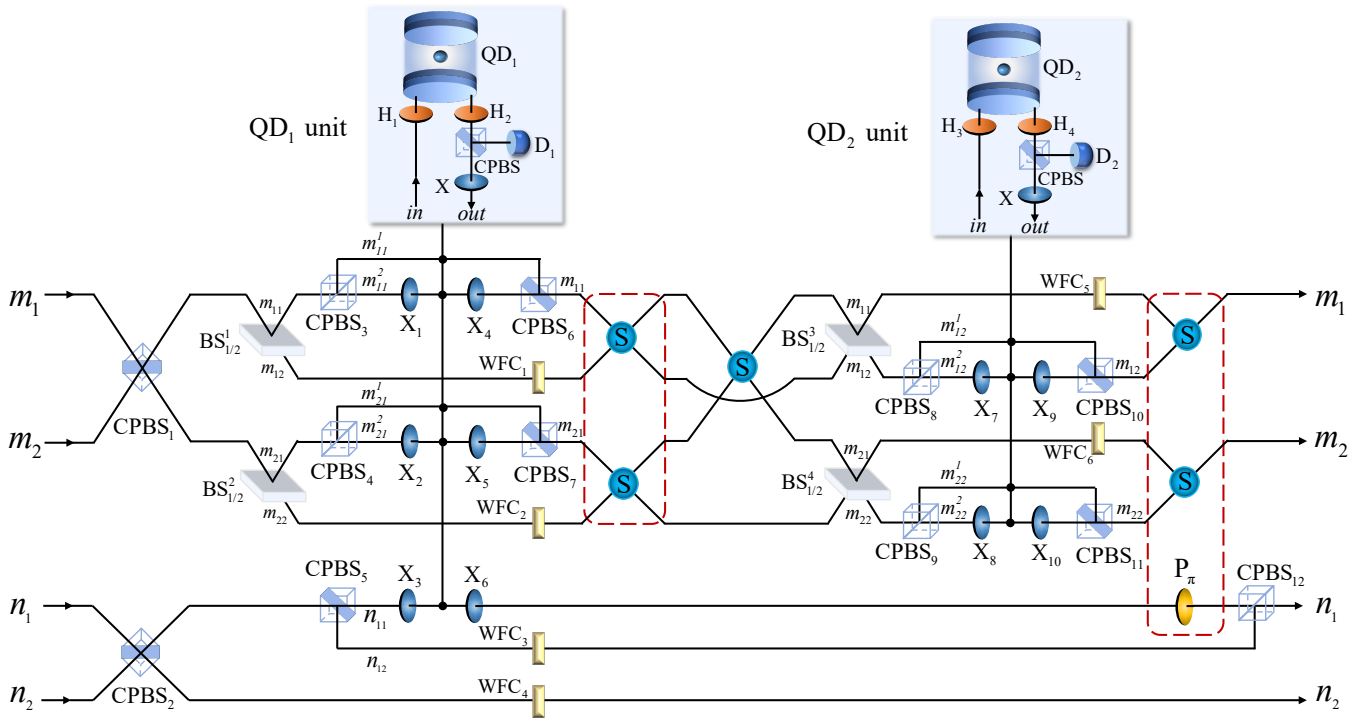

FIG. 3. Schematic diagram of the error-heralded 16D CSUM gate. WFC is a wave-form corrector that executes the coefficient variation $|R\rangle$ ($|L\rangle$) $\rightarrow A|R\rangle(|L\rangle)$. Half-wave plate H_i $(i = 1, 2, 3, 4)$ performs the Hadamard operation in polarized DoF.

states. Specifically, detector D_j detects a photon in the $|L\rangle$ output state upon reflection by the CPBS, indicating a fault. However, the spin state of the microcavity-QD_j system retains its integrity and remains reusable in subsequent cycles. The polarization-dependent selection imposed by the CPBS suppresses errors stemming from imperfect photon-spin interactions within the microcavity-QD_j system. Conversely, a photon in the $|R\rangle$ output state propagates directly through the CPBS and subsequently passes through an X-polarization converter, yielding the final desired outcome

$$|L\rangle|+\rangle \rightarrow A|L\rangle|-\rangle. \tag{15}$$

Thus, assuming identical initial states for both gates, the states in each expression of the error-heralded deterministic 16D CSUM gate, corresponding to the deterministic 16D CSUM gate assisted by the one-sided microcavity-QD system, are

$$|\mathrm{CSUM}^{'}\rangle = \mathrm{A}^3|\Phi_7\rangle. \tag{16}$$

V. DISCUSSION ON THE FIDELITY AND EFFICIENCY OF EACH PROTOCOL

The first protocol relies solely on linear optical elements, including CPBSs and BSs. Experimentally, CPBS may be substituted with calcite beam displacer (BD), as both optical components direct photons into different spatial modes based on their polarization states. Thus, upon the photon passes through the first CPBS, misalignments in mirror mounts (ϕ) and the polarization extinction ratio (p) result in deviations of the actual quantum state from the ideal input state. Consequently, the mode transformation matrix, applied to the two creation operators and influenced by ϕ and p, is expressed as [77]

$$\hat{U}^1_{\mathrm{CPBS}} = \hat{U}_p\hat{U}_\phi = \begin{bmatrix} \frac{1}{\sqrt{1+p}} & \frac{\sqrt{p}}{\sqrt{1+p}} \\ \frac{-\sqrt{p}^*}{\sqrt{1+p}} & \frac{1}{\sqrt{1+p}} \end{bmatrix} \begin{bmatrix} \cos\phi & \sin\phi \\ -\sin\phi & \cos\phi \end{bmatrix}, \tag{17}$$

$\sqrt{p}^*$ denotes the conjugate complex of $\sqrt{p}$. Assume that the input state is $|R\rangle$ or $|L\rangle$, the fidelity is given by

$$\begin{aligned} \mathcal{F}_R &= |\langle\varphi_{\mathrm{real}}|\varphi_{\mathrm{ideal}}\rangle|^2 = \frac{1}{1+p}\left|\cos\phi - \sqrt{r}\sin\phi\right|^2, \\ \mathcal{F}_L &= |\langle\varphi_{\mathrm{real}}|\varphi_{\mathrm{ideal}}\rangle|^2 = \frac{1}{1+p}\left|-\sqrt{r}^*\sin\phi + \cos\phi\right|^2. \end{aligned} \tag{18}$$

By analyzing Eq. (18), it is determined that $\mathcal{F}_R = \mathcal{F}_L$. Consequently, the fidelity of the first CPBS, denoted as $\mathcal{F}^1_{\mathrm{CPBS}}$, is given by $\frac{1}{1+p}\left|\cos\phi - \sqrt{p}\sin\phi\right|^2$.

For simplicity, it is assumed that the second CPBS and the first CPBS exhibit an identical extinction ratio. Ideally, the unitary mode transformation matrix of the second CPBS constitutes the inverse of the transforma-

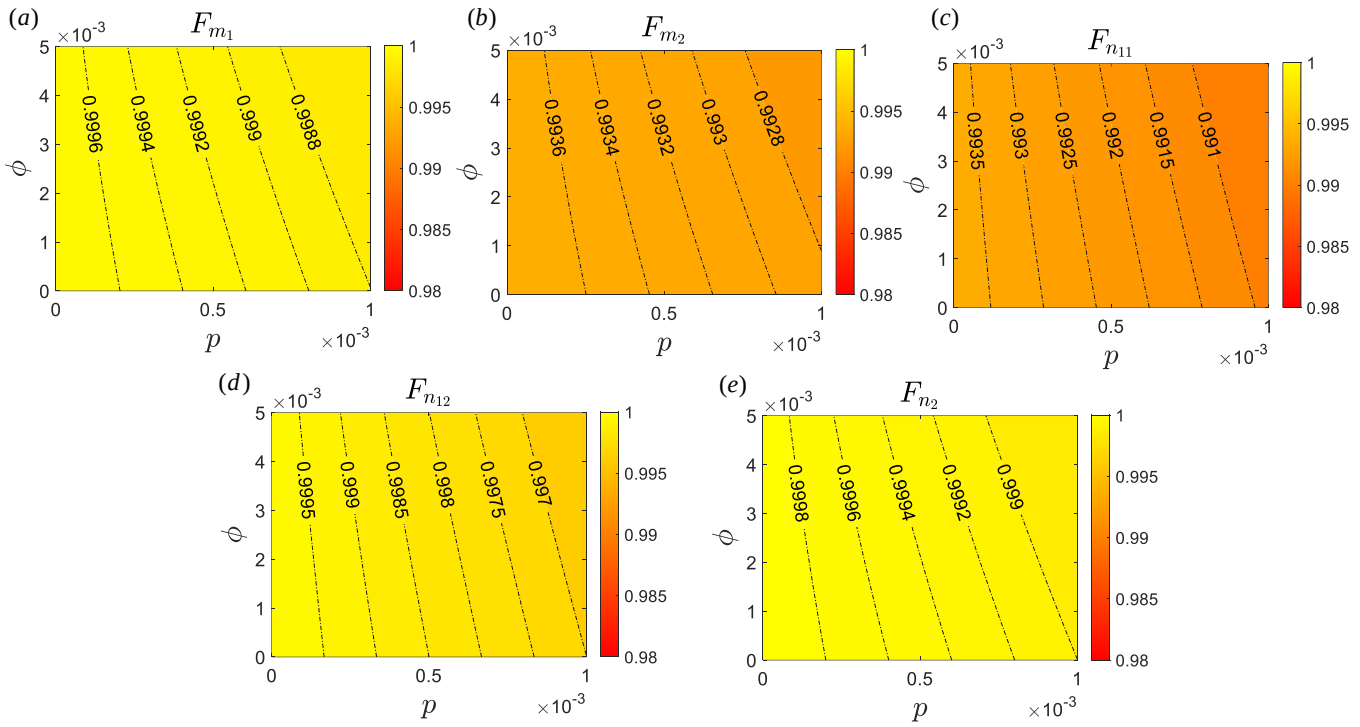

FIG. 4. The fidelity of (a) photon M in path m_1 (b) photon M in path m_2 (c) photon N in path n_{11} (d) photon N in path n_{12} (e) photon N in path n_2 vs the deviation in mirror mounts ϕ and the polarization extinction ratio p under realistic conditions $\Delta = \pi/36$ and $\xi = 0.02$.

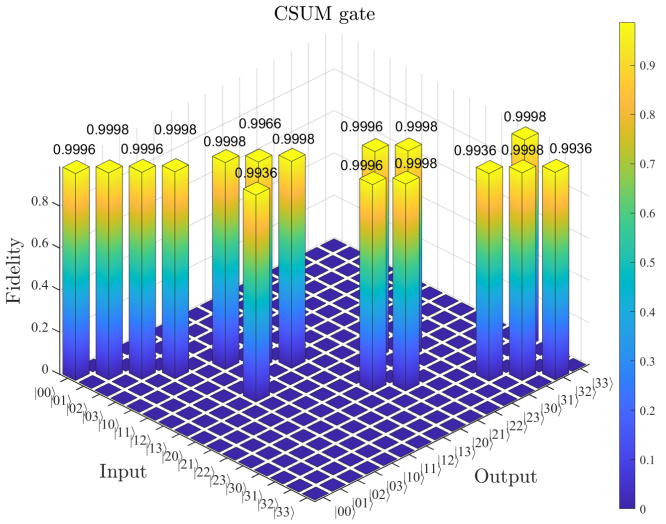

FIG. 5. The fidelity of the first protocol under realistic conditions $\Delta = \pi/36$, $\xi = 0.02$, $\phi = 0.001$ and $p = 0.0001$.

tion matrix of the first CPBS rotated by 90°, i.e.,

$$\hat{U}'_p = \frac{1}{\sqrt{1+p}} \begin{bmatrix} 1 & \sqrt{p}^* \\ -\sqrt{p} & 1 \end{bmatrix}. \tag{19}$$

In this step, the angle of deviation of the mirror mounts is not reconsidered, as the first CPBS and second CPBS are typically assembled with a consistent orientation. Consequently, by the definition of fidelity

$$\mathcal{F}^2_{\mathrm{CPBS}} = \mathcal{F}'_R = \mathcal{F}'_L = |\langle\varphi_{\mathrm{real}}|\varphi_{\mathrm{ideal}}\rangle|^2 = \frac{1}{1+p}. \tag{20}$$

The interference network formed by the combination of $\mathrm{BSs}_{1/2}$ and $\mathrm{BSs}_{1/3}$ essentially constitutes a Mach-Zehnder interferometer (MZI). If the actual phase difference between the two arms of the MZI is given by $\pi - \Delta$, the unitary transformation matrix describing the internal phase-shifting element is expressed as

$$\hat{U}_{\pi-\Delta} = \begin{bmatrix} e^{i(\pi-\Delta)} & 0 \\ 0 & 1 \end{bmatrix}. \tag{21}$$

Assuming a small deviation from ideal transmittance in $\mathrm{BS}_{1/2}$, the unitary transformation matrix of the $\mathrm{BS}_{1/2}$ is

$$\hat{U}_{\mathrm{BS}_{1/2}} = \frac{1}{\sqrt{\xi^2+2\xi+2}} \begin{bmatrix} 1+\xi & i \\ i & 1+\xi \end{bmatrix}. \tag{22}$$

where ξ denotes the imperfection in the transmission ratio. Consequently, the fidelity of $\mathrm{BS}_{1/2}$ is

$$\mathcal{F}_{\mathrm{BS}_{1/2}} = |\langle\varphi_{\mathrm{real}}|\varphi_{\mathrm{ideal}}\rangle|^2 = \frac{(\xi+2)^2}{2\,(\xi^2+2\xi+2)}. \tag{23}$$

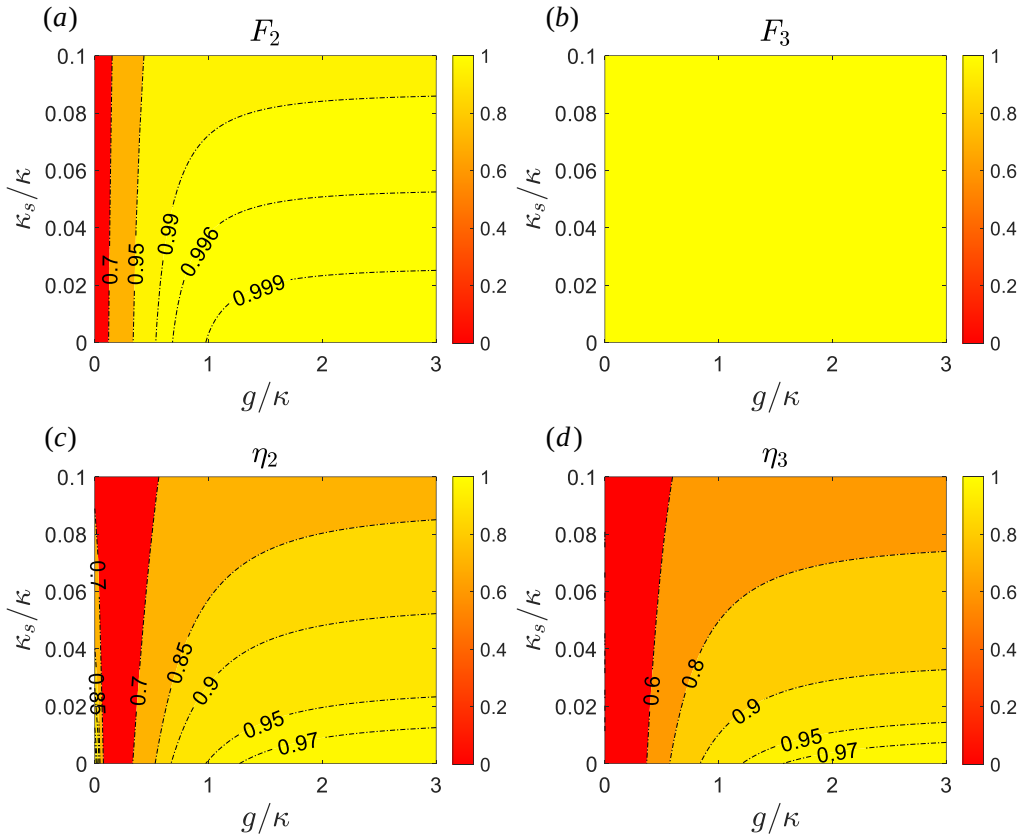

FIG. 6. (a) the fidelity F_2 of the second protocol (b) the fidelity F_3 of the third protocol (ignoring photon loss) (c) the efficiency η_2 of the second protocol (d) the efficiency η_3 of the third protocol vs the side leakage rate κ_s/κ and the coupling strength g/κ with $\gamma = 0.1\kappa$.

Then the unitary transformation matrix for an imperfect MZI becomes

$$\hat{U}_{\rm MZI} = \hat{U}_{\rm BS_{1/2}}\hat{U}_{\pi-\Delta}\hat{U}_{\rm BS_{1/2}} = \frac{1}{\xi^2+2\xi+2} \begin{bmatrix} e^{i(\pi-\Delta)}(1+\xi)^2-1 & i(1+\xi)(e^{i(\pi-\Delta)}+1) \\ i(1+\xi)(e^{i(\pi-\Delta)}-1) & -e^{i(\pi-\Delta)}+(1+\xi)^2 \end{bmatrix}. \tag{24}$$

The fidelity of MZI is then given by

$$\mathcal{F}_{\rm MZI} = |\langle\varphi_{\rm real}|\varphi_{\rm ideal}\rangle|^2 = \frac{(1+\cos(\Delta))\left[(1+\xi)^2+1\right]^2}{2\left(\xi^2+2\xi+2\right)^2}. \tag{25}$$

The $\mathrm{BS}^1_{1/3}$, $\mathrm{BS}^3_{1/3}$, and $\mathrm{BS}^4_{1/3}$ only serves to balance the losses, and thus its impact on the overall fidelity can be considered negligible.

We calculate the fidelity of the first protocol based on linear elements encountered by the photon in different paths. The fidelity of photon M in path m_1 can be expressed as

$$\begin{aligned} F_{m_1} &= \mathcal{F}^1_{\rm CPBS}\mathcal{F}^2_{\rm BS_{1/2}} \\ &= \frac{|\cos\phi-\sqrt{r}\sin\phi|^2}{1+p}\frac{(\xi+2)^4}{4\left(\xi^2+2\xi+2\right)^2}. \end{aligned} \tag{26}$$

The fidelity of photon M in path m_2 can be expressed as

$$\begin{aligned} F_{m_2} &= \mathcal{F}^1_{\rm CPBS}\mathcal{F}_{\rm MZI} \\ &= \frac{|\cos\phi-\sqrt{r}\sin\phi|^2}{1+p} \\ &\quad \frac{(1+\cos(\Delta))\left[(1+\xi)^2+1\right]^2}{2\left(\xi^2+2\xi+2\right)^2}. \end{aligned} \tag{27}$$

The fidelity of photon N in path n_{11} can be expressed as

$$\begin{aligned} F_{n_{11}} &= (\mathcal{F}^1_{\rm CPBS})^2\mathcal{F}^2_{\rm CPBS}\mathcal{F}_{\rm MZI} \\ &= \frac{|\cos\phi-\sqrt{r}\sin\phi|^4}{(1+p)^3} \\ &\quad \frac{(1+\cos(\Delta))\left[(1+\xi)^2+1\right]^2}{2\left(\xi^2+2\xi+2\right)^2}. \end{aligned} \tag{28}$$

The fidelity of photon N in path n_{12} can be expressed as

$$\begin{aligned} F_{n_{12}} &= (\mathcal{F}^1_{\rm CPBS})^2\mathcal{F}^2_{\rm CPBS} \\ &= \frac{|\cos\phi-\sqrt{r}\sin\phi|^4}{(1+p)^3}. \end{aligned} \tag{29}$$

The fidelity of photon N in path n_2 can be expressed as

$$\begin{aligned} F_{n_2} &= \mathcal{F}^1_{\mathrm{CPBS}} \\ &= \frac{\left|\cos\phi - \sqrt{r}\sin\phi\right|^2}{1+p}. \end{aligned} \tag{30}$$

Assuming realistic conditions $\Delta = \pi/36$ and $\xi = 0.02$, the fidelities F_{m_1}, F_{m_2}, $F_{n_{11}}$, $F_{n_{12}}$, F_{n_2} are shown in Figs. 4(a)-(e), respectively. When linear optical elements exhibit defects or nonidealities, i.e., delay error $\Delta = \pi/36$, imperfection of the transmission ratio $\xi = 0.02$, the deviation in mirror mounts $\phi = 0.001$, and the polarization extinction ratio $p = 0.0001$, the fidelity of the first protocol is calculated to be greater than 0.9936 with 16 computational basis as shown in Fig. 5.

For the second protocol that present the deterministic 16D CSUM gate, assuming that the side leakage rate κ_s is negligible, the theoretical fidelity can reach unity in perfect microcavity system. However, to present the more realistic scenario, the influence of κ_s must be considered. The side leakage rate κ_s affects the amplitude of the reflected photon, which, in turn, impacts the fidelity F_2 and efficiency η_2 of the 16D CSUM gate. For the error-heralded 16D CSUM gate of the third protocol, the two QD_1 and QD_2 units have the error-heralded mechanism during imperfect photon scattering process. Errors arising from non-ideal scattering are filtered by the CPBSs. For example, the CPBS of the QD_j unit passively filters out the incorrect $|L\rangle$ state components while transmitting the useful $|R\rangle$ state components to X. The response of D is solely used to indicate the presence of error. As a result, the fidelity F_3 of the error-heralded deterministic 16D CSUM gate shown in Eq. (16), can theoretically approach unity (ignoring photon loss) as shown in Fig. 6 (b), but impacts its efficiency η_3, leading to lower than the efficiency η_2. In a word, the cavity decay rate ratio κ_s/κ and the coupling strength ratio g/κ significantly influence the efficiency η_2 and η_3 of both two protocols and fidelity F_2 of the second protocol, but not affect the fidelity F_3 of the third protocol. In practical experiments, a value of $\gamma = 0.1\kappa$ is achievable. Specifically, the analyses of the fidelities and efficiencies reveal that they are improved as g/κ increases and κ_s/κ decreases in Fig. 6. For instance, when g/κ increases from 1.2 to 2.4, F_2, η_2, and η_3 improve from 0.9995, 0.9670, and 0.9506 to 0.9999, 0.9913, and 0.9870, respectively, while maintaining a constant $\kappa_s/\kappa = 0$. Conversely, when κ_s/κ increases from 0 to 0.05 while keeping $g/\kappa = 2.4$, F_2, η_2, and η_3 decrease from 0.9999, 0.9913, and 0.9870 to 0.9961, 0.8998, and 0.8508, respectively.

In practical implementations, achieving strong coupling represents a prerequisite for robust-fidelity 16D gate operation. Strong coupling has been experimentally demonstrated in cavity-QD_j systems, including micropillar structures, microdisk configurations, and QD-nanocavity architectures. In 2011, Hu *et al.* reported $g/\kappa \approx 2.4$ in a micropillar cavity featuring $\kappa_s/\kappa \approx 0$ and a quality factor $Q \approx 4 \times 10^4$. Fig. 7 illustrates the fidelities of 16 computational basis states resulting from the application of the second protocol for two photons in two DoFs, against 16D input states under the parameters $g/\kappa = 2.4$, $\kappa_s/\kappa = 0$, and $\gamma = 0.1\kappa$. As evidenced, the fidelity for each computational basis exceeds 0.9999.

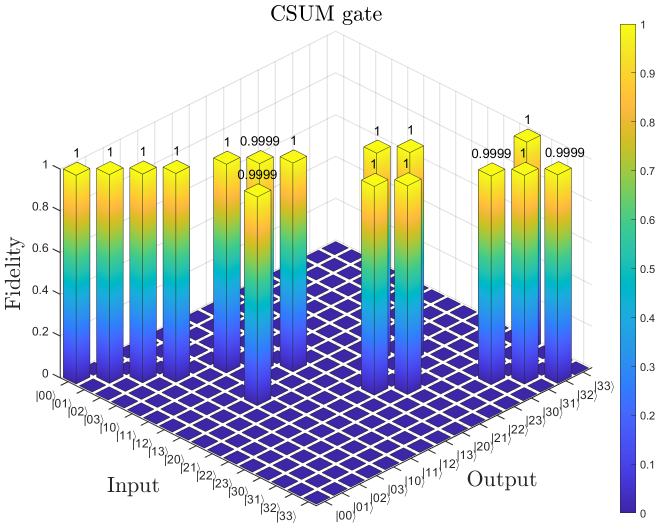

FIG. 7. The fidelity of the second protocol with computational basis under the condition $g/\kappa = 2.4$, $\kappa_s/\kappa = 0$ and $\gamma = 0.1\kappa$.

VI. SUMMARY

In summary, we propose three practical protocols for realizing the 16D CSUM gate. The first protocol solely relies on linear optical elements, with current optical technologies, yielding the efficiency η_1 of 1/9 and the fidelity F_1 greater than 0.9936 under realistic conditions delay error $\Delta = \pi/36$, imperfection of the transmission ratio $\xi = 0.02$, deviation in mirror mounts $\phi = 0.001$, and polarization extinction ratio $p = 0.0001$. The second protocol utilizes the photon scattering characteristics of the microcavity-QD system with the efficiency η_2 of 0.9913 and the fidelity F_2 of 0.9999 keeping the condition side leakage rate $\kappa_s/\kappa = 0$ and coupling strength $g/\kappa = 2.4$. As the error-heralded mechanism is incorporated for the third protocol, under the same condition as the second protocol, its efficiency η_3 of 0.9870 and fidelity F_3 of 1. Moreover, this encoding strategy of the 16D CSUM gates reduce resource overhead, suppress decoherence, and shorten operational timescales, thereby facilitating efficient storage and enabling ultrafast QIP. The proposed protocols provide a scalable framework for advancing HD quantum computing, delivering enhanced processing capabilities and robust performance.

ACKNOWLEDGMENTS

This work was supported in part by the Natural Science Foundation of China under Contract 61901420; in part by Fundamental Research Program of Shanxi Province under Contract 20230302121116.

DISCLOSURES

The authors declare no conflicts of interest.

DATA AVAILABILITY STATEMENT

Data underlying the results presented in this paper are not publicly available at this time but may be obtained from the authors upon reasonable request.

[1] L. Gyongyosi and S. Imre, A survey on quantum computing technology, Comput. Sci. Rev. **31**, 51 (2019).

[2] M. Agnew, J. Leach, M. McLaren, F. S. Roux, and R. W. Boyd, Tomography of the quantum state of photons entangled in high dimensions, Phys. Rev. A **84**, 062101 (2011).

[3] M. Krenn, M. Huber, R. Fickler, R. Lapkiewicz, S. Ramelow, and A. Zeilinger, Generation and confirmation of a (100 × 100)-dimensional entangled quantum system, PNAS **111**, 6243 (2014).

[4] Y. Zhang, F. S. Roux, T. Konrad, M. Agnew, J. Leach, and A. Forbes, Engineering two-photon high-dimensional states through quantum interference, Sci. Adv. **2**, e1501165 (2016).

[5] M. Malik, M. Erhard, M. Huber, R. F. Mario Krenn, and A. Zeilinger, Multi-photon entanglement in high dimensions, Nat. Photonics **10**, 248 (2016).

[6] J. Li, Z. Xie, Y. Li, Y. Liang, Z. Li, and T. Li, Heralded entanglement between error-protected logical qubits for fault-tolerant distributed quantum computing, Science China Physics, Mechanics & Astronomy **67**, 220311 (2024).

[7] B. C. Ren, G. Y. Wang, and F. G. Deng, Universal hyperparallel hybrid photonic quantum gates with dipole-induced transparency in the weak-coupling regime, Phys. Rev. A **91**, 032328 (2015).

[8] T. Li and G. L. Long, Hyperparallel optical quantum computation assisted by atomic ensembles embedded in double-sided optical cavities, Phys. Rev. A **94**, 022343 (2016).

[9] W. Su, W. Qin, A. Miranowicz, T. Li, and F. Nori, Heralded nonlocal quantum gates for distributed quantum computation in a decoherence-free subspace, Phys. Rev. A **110**, 052612 (2024).

[10] W. Q. Liu, H. R. Wei, and L. C. Kwek, Universal quantum multi-qubit entangling gates with auxiliary spaces, Adv. Quantum Technol. **5**, 2100136 (2022).

[11] W. Q. Liu and H. R. Wei, Linear optical universal quantum gates with higher success probabilities, Adv. Quantum Technol. **6**, 2300009 (2023).

[12] H. R. Wei, F. G. Deng, and G. L. Long, Hyper-parallel toffoli gate on three-photon system with two degrees of freedom assisted by single-sided optical microcavities, Opt. Express **24**, 18619 (2016).

[13] H. R. Wei and G. L. Long, Universal photonic quantum gates assisted by ancilla diamond nitrogen-vacancy centers coupled to resonators, Phys. Rev. A **91**, 032324 (2015).

[14] N. F. Gong, T. J. Wang, and S. Ghose, Control power of a high-dimensional controlled nonlocal quantum computation, Phys. Rev. A **103**, 052601 (2021).

[15] A. Crespi, R. Ramponi, R. Osellame, L. Sansoni, I. Bongioanni, F. Sciarrino, G. Vallone, and P. Mataloni, Integrated photonic quantum gates for polarization qubits, Nat. Commun. **2**, 566 (2011).

[16] R. Fickler, R. Lapkiewicz, W. N. Plick, M. Krenn, C. Schaeff, S. Ramelow, and A. Zeilinger, Quantum entanglement of high angular momenta, Science **338**, 640 (2012).

[17] M. Kues, C. Reimer, P. Roztocki, L. R. Cortés, S. Sciara, B. Wetzel, Y. Zhang, A. Cino, S. T. Chu, B. E. Little, D. J. Moss, L. Caspani, J. Azaña, and R. Morandotti, On-chip generation of high-dimensional entangled quantum states and their coherent control, Nature **546**, 622 (2017).

[18] A. Martin, T. Guerreiro, A. Tiranov, S. Designolle, F. Fröwis, N. Brunner, M. Huber, and N. Gisin, Quantifying photonic high-dimensional entanglement, Phys. Rev. Lett. **118**, 110501 (2017).

[19] N. Herrera Valencia, V. Srivastav, M. Pivoluska, M. Huber, N. Friis, W. McCutcheon, and M. Malik, High-dimensional pixel entanglement: Efficient generation and certification, Quantum **4**, 376 (2020).

[20] M. A. Nielsen, M. J. Bremner, J. L. Dodd, A. M. Childs, and C. M. Dawson, Universal simulation of hamiltonian dynamics for quantum systems with finite-dimensional state spaces, Phys. Rev. A **66**, 022317 (2002).

[21] A. D. Greentree, S. G. Schirmer, F. Green, L. C. L. Hollenberg, A. R. Hamilton, and R. G. Clark, Maximizing the hilbert space for a finite number of distinguishable quantum states, Phys. Rev. Lett. **92**, 097901 (2004).

[22] A. Sit, F. Bouchard, R. Fickler, J. Gagnon-Bischoff, H. Larocque, K. Heshami, D. Elser, C. Peuntinger, K. Günthner, B. Heim, C. Marquardt, G. Leuchs, R. W. Boyd, and E. Karimi, High-dimensional intracity quantum cryptography with structured photons, Optica **4**, 1006 (2017).

[23] P. B. Dixon, G. A. Howland, J. Schneeloch, and J. C. Howell, Quantum mutual information capacity for high-dimensional entangled states, Phys. Rev. Lett. **108**, 143603 (2012).

[24] S. Gröblacher, T. Jennewein, A. Vaziri, G. Weihs, and A. Zeilinger, Experimental quantum cryptography with qutrits, New J. Phys. **8**, 75 (2006).

[25] C. Zhang, Q. Zhang, W. Zhong, M. M. Du, S. T. Shen, X. Y. Li, A. L. Zhang, L. Zhou, and

Y. B. Sheng, Memory-assisted measurement-device-independent quantum secret sharing, Phys. Rev. A **111**, 012602 (2025).
[26] M. Mafu, A. Dudley, S. Goyal, D. Giovannini, M. McLaren, M. J. Padgett, T. Konrad, F. Petruccione, N. Lütkenhaus, and A. Forbes, Higher-dimensional orbital-angular-momentum-based quantum key distribution with mutually unbiased bases, Phys. Rev. A **88**, 032305 (2013).
[27] Q. Zhang, J. W. Ying, Z. J. Wang, W. Zhong, M. M. Du, S. T. Shen, X. Y. Li, A. L. Zhang, S. P. Gu, X. F. Wang, L. Zhou, and Y. B. Sheng, Device-independent quantum secret sharing with advanced random key generation basis, Phys. Rev. A **111**, 012603 (2025).
[28] W. Q. Liu and H. R. Wei, Quantum gate teleportation with the superposition of causal order, Phys. Rev. Appl. **23**, 014064 (2025).
[29] T. Li, Z. Gao, and K. Xia, Nonlinear-dissipation-induced nonreciprocal exceptional points, Opt. Express **29**, 17613 (2021).
[30] M. Mirhosseini, O. S. Magaña-Loaiza, M. N. O'Sullivan, B. Rodenburg, M. Malik, M. P. J. Lavery, M. J. Padgett, D. J. Gauthier, and R. W. Boyd, High-dimensional quantum cryptography with twisted light, New J. Phys. **17**, 033033 (2015).
[31] A. Bocharov, M. Roetteler, and K. M. Svore, Factoring with qutrits: Shor's algorithm on ternary and metaplectic quantum architectures, Phys. Rev. A **96**, 012306 (2017).
[32] M. Krenn, R. Fickler, M. Fink, J. Handsteiner, M. Malik, T. Scheidl, R. Ursin, and A. Zeilinger, Communication with spatially modulated light through turbulent air across vienna, New J. Phys. **16**, 113028 (2014).
[33] M. Krenn, J. Handsteiner, M. Fink, R. Fickler, R. Ursin, M. Malik, and A. Zeilinger, Twisted light transmission over 143 km, PNAS **113**, 13648 (2016).
[34] Y. Ren, Z. Wang, P. Liao, L. Li, G. Xie, H. Huang, Z. Zhao, Y. Yan, N. Ahmed, A. Willner, M. P. J. Lavery, N. Ashrafi, S. Ashrafi, R. Bock, M. Tur, I. B. Djordjevic, M. A. Neifeld, and A. E. Willner, Experimental characterization of a 400 gbit/s orbital angular momentum multiplexed free-space optical link over 120 m, Opt. Lett. **41**, 622 (2016).
[35] M. P. J. Lavery, C. Peuntinger, K. Günthner, P. Banzer, D. Elser, R. W. Boyd, M. J. Padgett, C. Marquardt, and G. Leuchs, Free-space propagation of high-dimensional structured optical fields in an urban environment, Sci. Adv. **3**, e1700552 (2017).
[36] B. P. Lanyon, M. Barbieri, M. P. Almeida, T. Jennewein, T. C. Ralph, K. J. Resch, G. J. Pryde, J. L. O'Brien, A. Gilchrist, and A. G. White, Simplifying quantum logic using higher-dimensional hilbert spaces, Nat. Phys. **5**, 134 (2009).
[37] M. Huber and M. Pawłowski, Weak randomness in device-independent quantum key distribution and the advantage of using high-dimensional entanglement, Phys. Rev. A **88**, 032309 (2013).
[38] G. Z. Song, L. X. Wang, J. X. Zhang, and H. R. Wei, Tunable photon scattering by an atom dimer coupled to a band edge of a photonic crystal waveguide, Phys. Rev. A **111**, 023707 (2025).
[39] C. Cao, L. Zhang, Y. H. Han, P. P. Yin, L. Fan, Y. W. Duan, and R. Zhang, Complete and faithful hyperentangled-bell-state analysis of photon systems using a failure-heralded and fidelity-robust quantum gate, Opt. Express **28**, 2857 (2020).
[40] F. Bouchard, R. Fickler, R. W. Boyd, and E. Karimi, High-dimensional quantum cloning and applications to quantum hacking, Sci. Adv. **3**, e1601915 (2017).
[41] L. Zhang, C. Silberhorn, and I. A. Walmsley, Secure quantum key distribution using continuous variables of single photons, Phys. Rev. Lett. **100**, 110504 (2008).
[42] F. Wang, P. Zeng, J. Zhao, B. Braverman, Y. Zhou, M. Mirhosseini, X. Wang, H. Gao, F. Li, R. W. Boyd, and P. Zhang, High-dimensional quantum key distribution based on mutually partially unbiased bases, Phys. Rev. A **101**, 032340 (2020).
[43] S. Massar, Nonlocality, closing the detection loophole, and communication complexity, Phys. Rev. A **65**, 032121 (2002).
[44] D. Collins, N. Gisin, N. Linden, S. Massar, and S. Popescu, Bell inequalities for arbitrarily high-dimensional systems, Phys. Rev. Lett. **88**, 040404 (2002).
[45] A. C. Dada, J. Leach, G. S. Buller, M. J. Padgett, and E. Andersson, Experimental high-dimensional two-photon entanglement and violations of generalized bell inequalities, Nat. Phys. **7**, 677 (2011).
[46] N. J. Cerf, M. Bourennane, A. Karlsson, and N. Gisin, Security of quantum key distribution using d-level systems, Phys. Rev. Lett. **88**, 127902 (2002).
[47] H. Bechmann-Pasquinucci and W. Tittel, Quantum cryptography using larger alphabets, Phys. Rev. A **61**, 062308 (2000).
[48] S. Ecker, F. Bouchard, L. Bulla, F. Brandt, O. Kohout, F. Steinlechner, R. Fickler, M. Malik, Y. Guryanova, R. Ursin, and M. Huber, Overcoming noise in entanglement distribution, Phys. Rev. X **9**, 041042 (2019).
[49] J. Bavaresco, N. H. Valencia, C. Klöckl, M. Pivoluska, P. Erker, N. Friis, M. Malik, and M. Huber, Measurements in two bases are sufficient for certifying high-dimensional entanglement, Nat. Phys. **14**, 1032 (2018).
[50] M. Krenn, J. Handsteiner, M. Fink, R. Fickler, and A. Zeilinger, Twisted photon entanglement through turbulent air across vienna, PNAS **112**, 14197 (2015).
[51] F. Bouchard, A. Sit, F. Hufnagel, A. Abbas, Y. Zhang, K. Heshami, R. Fickler, C. Marquardt, G. Leuchs, R. w. Boyd, and E. Karimi, Quantum cryptography with twisted photons through an outdoor underwater channel, Opt. Express **26**, 22563 (2018).
[52] Q. F. Zhang, Y. R. Zhou, F. F. Liu, X. Y. Wang, Y. P. Gao, L. Fan, and C. Cao, Magnon-squeezing-enhanced phonon lasering in cavity magnomechanics, Adv. Quantum Technol. **7**, 2400200 (2024).
[53] G. Vallone, E. Pomarico, F. De Martini, and P. Mataloni, Active one-way quantum computation with two-photon four-qubit cluster states, Phys. Rev. Lett. **100**, 160502 (2008).
[54] M. Pivoluska, M. Huber, and M. Malik, Layered quantum key distribution, Phys. Rev. A **97**, 032312 (2018).
[55] M. Doda, M. Huber, G. Murta, M. Pivoluska, M. Plesch, and C. Vlachou, Quantum key distribution overcoming extreme noise: Simultaneous subspace coding using high-dimensional entanglement, Phys. Rev. Appl. **15**, 034003 (2021).
[56] X. Y. Zhang, C. Cao, Y. P. Gao, L. Fan, R. Zhang, and C. Wang, Generation and manipulation of phonon lasering in a two-drive cavity magnomechanical system, New J. Phys. **25**, 053039 (2023).

[57] Y. Wang, Z. Hu, B. C. Sanders, and S. Kais, Qudits and high-dimensional quantum computing, Front. Phys. **8**, 589504 (2020).

[58] E. O. Kiktenko, A. S. Nikolaeva, P. Xu, G. V. Shlyapnikov, and A. K. Fedorov, Scalable quantum computing with qudits on a graph, Phys. Rev. A **101**, 022304 (2020).

[59] A. S. Nikolaeva, E. O. Kiktenko, and A. K. Fedorov, Efficient realization of quantum algorithms with qudits, EPJ Quantum Technol. **11**, 43 (2024).

[60] G. Vidal, Efficient classical simulation of slightly entangled quantum computations, Phys. Rev. Lett. **91**, 147902 (2003).

[61] R. Jozsa and N. Linden, On the role of entanglement in quantum-computational speed-up, PNAS **459**, 2011 (2003).

[62] L. Sheridan and V. Scarani, Security proof for quantum key distribution using qudit systems, Phys. Rev. A **82**, 030301 (2010).

[63] E. T. Campbell, Enhanced fault-tolerant quantum computing in d-level systems, Phys. Rev. Lett. **113**, 230501 (2014).

[64] F. H. E. Watson, H. Anwar, and D. E. Browne, Fast fault-tolerant decoder for qubit and qudit surface codes, Phys. Rev. A **92**, 032309 (2015).

[65] Q. Wang, D. Lyu, J. Liu, and J. Wang, Polarization and orbital angular momentum encoded quantum toffoli gate enabled by diffractive neural networks, Phys. Rev. Lett. **133**, 140601 (2024).

[66] P. C. Humphreys, B. J. Metcalf, J. B. Spring, M. Moore, X.-M. Jin, M. Barbieri, W. S. Kolthammer, and I. A. Walmsley, Linear optical quantum computing in a single spatial mode, Phys. Rev. Lett. **111**, 150501 (2013).

[67] P. Maunz, S. Olmschenk, D. Hayes, D. N. Matsukevich, L. M. Duan, and C. Monroe, Heralded quantum gate between remote quantum memories, Phys. Rev. Lett. **102**, 250502 (2009).

[68] A. Crespi, R. Ramponi, R. Osellame, L. Sansoni, I. Bongioanni, F. Sciarrino, G. Vallone, and P. Mataloni, Integrated photonic quantum gates for polarization qubits, Nat. Commun. **2**, 566 (2011).

[69] D. F. Urrego, D. Lopez-Mago, V. V. na Hernández, and J. P. Torres, Quantum-inspired fredkin gate based on spatial modes of light, Opt. Express **28**, 12661 (2020).

[70] S. Gasparoni, J.-W. Pan, P. Walther, T. Rudolph, and A. Zeilinger, Realization of a photonic controlled-not gate sufficient for quantum computation, Phys. Rev. Lett. **93**, 020504 (2004).

[71] P. Imany, J. A. Jaramillo-Villegas, M. S. Alshaykh, J. M. Lukens, O. D. Odele, A. J. Moore, D. E. Leaird, M. Qi, and A. M. Weiner, High-dimensional optical quantum logic in large operational spaces, npj Quantum Inf. **5**, 59 (2019).

[72] X. Gao, M. Erhard, A. Zeilinger, and M. Krenn, Computer-inspired concept for high-dimensional multipartite quantum gates, Phys. Rev. Lett. **125**, 050501 (2020).

[73] Q. P. Su, Y. Zhang, L. Bin, and C. P. Yang, Hybrid controlled-sum gate with one superconducting qutrit and one cat-state qutrit and application in hybrid entangled state preparation, Phys. Rev. A **105**, 042434 (2022).

[74] Z. Meng, W. Q. Liu, B. W. Song, X. Y. Wang, A. N. Zhang, and Z. Q. Yin, Experimental realization of high-dimensional quantum gates with ultrahigh fidelity and efficiency, Phys. Rev. A **109**, 022612 (2024).

[75] T. C. Ralph, K. J. Resch, and A. Gilchrist, Efficient toffoli gates using qudits, Phys. Rev. A **75**, 022313 (2007).

[76] H. F. Hofmann and S. Takeuchi, Quantum phase gate for photonic qubits using only beam splitters and postselection, Phys. Rev. A **66**, 024308 (2002).

[77] H. Meng, Deterministic linear-optical quantum control gates utilizing path and polarization degrees of freedom, Phys. Rev. A **105**, 032607 (2022).